

# A Chemical Approach to the First-Principles Modeling of Novel Thermoelectric Materials

---

Luca Bertini,  
Fausto Cargnoni,  
and Carlo Gatti

*CNR-ISTM, Istituto di Scienze  
e Tecnologie Molecolari*

7.1	Introduction .....	7-1
7.2	Charge Transfer, Charge Donation, and Chemical Bonding in Type I Inorganic Clathrates .....	7-2
7.3	Theoretical Modeling for Optimal Doping Elements and Doping Level in $\text{Co}_4\text{Sb}_{12}$ .....	7-6
7.4	A Combined Theoretical and Experimental Structural Study of $\beta$ Zn–Sb .....	7-10

## 7.1 Introduction

---

Competitive thermoelectric (TE) materials have a high figure-of-merit  $ZT$ , defined as  $ZT = (\alpha^2 \sigma / \lambda) T$ . The Seebeck coefficient  $\alpha$ , the electrical conductivity  $\sigma$ , and the total thermal conductivity  $\lambda$  (given by the sum of the lattice and the electronic contributions  $\lambda_L$  and  $\lambda_e$ ) are all dependent on the material's composition, atomic arrangement, and electronic band structure. Generally speaking, these systems may be studied either emphasizing the *band* structure view typical of physicists or the *chemical bond* view typical of chemists. The authors try to combine these two perspectives in this chapter wherever it is possible and convenient. Native defects, doping, and nanostructuring may affect significantly the properties of the TE materials. In some cases, it is possible to account for these effects either by studying the perturbations they induce on the electronic band structure of a regularly periodic system, or by viewing the defect as a real space local modification both of the crystal atomic structure and of the bonding network.

Most experimental techniques used to study the geometric and electronic structure of bulk materials obtain space–time averages over either the entire sample or a nanoscale portion of it. The positional disorder and native defects of TE materials fundamentally affect the interpretation of experimental information, and therefore deconvolution is necessary to gain an understanding of the relationship between the local structural arrangement of the crystal cells and bulk transport properties. In this respect, the theoretical modeling is a useful tool when combined with experimental evidence. Examples will be provided later in this chapter. First the role of guest–host interactions in type I inorganic clathrates is discussed. Second, the theoretical modeling of doping in  $\text{Co}_4\text{Sb}_{12}$  skutterudites is presented.

Finally, the recovery of the atomistic structure of a disordered material, the  $\beta$  phase of zinc antimonides (by combining an experimental x-rays diffraction (XRD) study and theoretical computations) is outlined.

Investigative tools proper of to solid-state physics or of chemistry were employed. The electronic band structure of these materials was obtained by fully periodic computations, using the density functional theory within the linear combination of atomic orbitals formalism, as implemented in the CRYSTAL98 code.<sup>1</sup>

Gradient-corrected density functionals and Gaussian basis sets especially designed for each system were used. In general, both the electronic structure of the ideal crystal and of its defective modifications were computed in order to determine from first principles the relationships between doping elements, local defective structures, and electronic transport properties. These latter were evaluated as a continuum function of the charge carriers concentration, using the Boltzmann's semiclassical formalism.<sup>2</sup> We applied the frozen band approximation to the electronic bands of the unperturbed crystals or to those of the fully doped defective systems. These calculations were performed with the ELTRAP<sup>3</sup> code, interfaced with CRYSTAL98. The frozen band approximation accounts for the actual doping level by filling or "emptying out" the electronic bands of the reference system and it is more accurate at lower doping levels.

Another model was examined which complements the above-cited approaches, and which reflects more closely the view of chemists. This model is based on direct space analysis of the material's electron density distribution (EDD) according to the formalism of the quantum theory of atoms in molecules (QTAIM).<sup>4</sup> This theory is rooted in quantum mechanics, it defines atomic subsystems whose properties are determined by physics and makes no use of any Hilbert space partitioning to extract information from the wave function. More importantly, the QTAIM derives the concepts of atom and bond, which are cornerstones of chemical thinking, on an unambiguous basis. The QTAIM analysis was carried out using the TOPOND98 code,<sup>5</sup> interfaced with CRYSTAL98.

## 7.2 Charge Transfer, Charge Donation, and Chemical Bonding in Type I Inorganic Clathrates

Recently, thermoelectric materials with open framework structures have aroused a surge of interest since these structures have the potential to possess the ideal thermoelectric properties of a phonon glass and an electron single crystal (PGEC) recently introduced by Slack.<sup>6</sup> Interest has focused on inorganic clathrates, whose electronic and thermal transport properties can be influenced and perhaps tuned by subtle changes in structural details and chemical substitution.<sup>7</sup>

Type I clathrates consist of two kind of cages, the 20-atom dodecahedron and the 24-atom tetrakaidecahedral cages (Figure 7.1), which encapsulate guest metal atoms M and are generally formed by Group 13 and Group 14 elements. All known clathrate type I structures exhibit a common total number of 184 valence electrons per unit cell, despite the large number of elemental compositions forming these structures. Hence, structural chemists generally regard these clathrates as Zintl phases, in which the guest atoms completely donate their valence electron to the framework. This electron flow fills the electron holes created by substitution of Group 14 for Group 13 elements in the tetrahedrally coordinated framework, thereby ensuring semiconductor-like properties to the clathrate when undoped. Recent studies on  $A_8Ga_{16}Ge_{30}$  ( $A = Sr, Ba$ ), based on theoretical EDD<sup>8</sup> or maximum-entropy method (MEM) analysis of experimental EDD,<sup>9</sup> have however disputed the ionic character of the guest atoms and rather supported the idea of nonionic metal guests in these clathrates. XANES data at the Sr K-edge seem to corroborate this startling result, since they revealed an edge position for the clathrate close to that of Sr metal, although the adsorption edge was very broad.<sup>9</sup> The neutral character of guest atoms appears clearly inconsistent with their role as electron donors, which was admittedly demonstrated by the same band structure calculations from which the theoretical EDD was derived.<sup>8</sup> Conversely, it was also noted that guests atoms were generally found far off the cage center and with displacements and vibrational frequencies which differed from guest to guest and, for a given guest, from the large to the small cage.

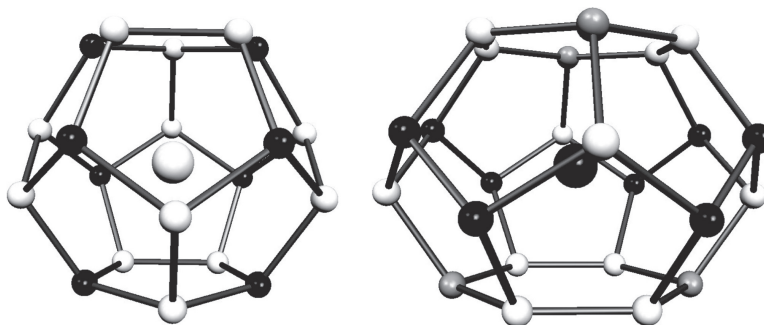


**FIGURE 7.1** The 20-atom (left) and the 24-atom (right) cages of the clathrate type I structure. Atomic special positions are labeled according to the  $Pm-3n$  space group of the idealized and fully symmetric  $A_8Ga_{16}Ge_{30}$  clathrate. Within this group, there are only three types of framework sites (6c, gray, 16i, black and 24k, white) and two different locations (2a, white, and 6d, black large circles) for the guest atoms at the center of the 20-atom and 24-atom cages, respectively. Minimum energy clathrates belong to the P1 space group and retain similar atomic arrangements, but with guest atoms significantly displaced from the center of cages.

According to Blake et al.<sup>8</sup> and Bentien et al.,<sup>9,10</sup> this may indicate a partially directional covalent guest—framework interaction, with consequent incomplete charge transfer (CT) between the guest and the host.<sup>8–10</sup> We believe that application of a rigorous, quantum-mechanically grounded theory, like QTAIM, could help clarifying this puzzling and seemingly “clashing picture” for the guest–host interactions in clathrates.<sup>11</sup> Table 7.1 shows QTAIM net charges for the guest atoms in  $A_8Ga_{16}Ge_{30}$  ( $A = Sr, Ba$ ) for the most stable P1 space group optimized structure of each clathrate. This structure has three Ga atoms in the 6c positions of the exagonal rings (Figure 7.1, position labeling according to the  $Pm-3n$  space group) and no unfavorable Ga–Ga bonds.<sup>8</sup> Guest atoms in clathrates appear as almost completely ionized regardless of the kind of cage they occupy. Their net charges of about 1.7e are very similar to those found for the corresponding atoms in the SrO and BaO oxides, which are both known to be paradigmatic ionic compounds. A very similar net charge for the guest atoms — not reported in Table 7.1 — was obtained<sup>11</sup> for the second more stable clathrate structures,<sup>8</sup> which had five Ga atoms in the favored  $sp^2$  symmetry 6c positions, but also four unfavorable Ga–Ga bonds.

This very stable and clear-cut description<sup>11</sup> of guest–host CT in clathrates raises the question of why QTAIM results contradict previous estimates from theory and experiment. QTAIM net atomic charges are obtained by evaluating the total net charge contained in a basin enclosing the nucleus and bounded by

**TABLE 7.1** Average QTAIM Net Charges (Standard Deviations) of Guest Atoms A,  $q(A)$ , in  $A_8Ga_{16}Ge_{30}$  ( $A = Sr, Ba$ ) Clathrates for *Ab Initio* and Independent Atom Model (IAM) Electron Densities

System/Model	A	$q(A)^a$	$q'(A)^b$
Clathrate/ <i>ab initio</i>	Sr	1.669 (0.001)	1.687 (0.005)
	Ba	1.743 (0.001)	1.773 (0.003)
Clathrate/IAM <sup>c</sup>	Sr	−0.096	−0.126
	Ba	0.858	0.576
AO/ <i>ab initio</i> <sup>d</sup>	Sr		1.717
	Ba		1.758

Data from Ref. [11], at *ab initio* minimum energy geometry.<sup>8</sup> Data (Ref. [11]) for AO ( $A = Sr, Ba$ ) oxides are listed for the sake of comparison.

<sup>a</sup> 20 atom cage for clathrates.

<sup>b</sup> 24 atom cage for clathrates.

<sup>c</sup> IAM computations at the  $Pm-3n$  space group geometry, Ref. [11].

<sup>d</sup> T2 test, Ref. [11].

a surface whose points have zero flux for the gradient of the density.<sup>4</sup> This ensures that the resulting basins are quantum objects, ones whose properties are defined by physics. Common to previous studies was the adoption of a CT definition which (rather than identifying the electronic charge atomic catchment basins, and hence the net atomic charges based on quantum mechanics for open systems), was simply based on the rearrangement of the EDD respect to a given reference density. This was the density of the interleaved, noninteracting  $A_8$  and  $Ga_{16}Ge_{30}$  sublattices in the theoretical study<sup>8</sup> and the nonuniform prior density in the MEM experimental analysis.<sup>9</sup> In both cases, charges on a given guest atom in the clathrate and in the reference system were calculated by evaluating the total electron charge within a sphere of a given radius around a given guest atom and were found to be similar. However, charge partitioning among atoms is not simply a matter of geometrical position, but rather of the physical properties that are associated with such a position. If the interaction among atoms constituting a system is switched on, the properties at a given point vary. The electron density at this point may no longer be apportioned to the same atom as when the interaction is switched off. Although the independent atom model (IAM) density, the sum of undistorted atomic densities, is not a quantum object, the QTAIM recipe may still be applied. In this case, the guest atoms in the clathrates turn out to be much less ionized, with Sr atoms being close to neutrality and Ba atoms being less than half-charged (Table 7.1).<sup>11</sup> While physics does not require that the zero-flux recipe should predict the A atoms to be neutral for IAM densities, it is nonetheless interesting that this recipe predicts very small or small net charges when the interaction among atoms is switched off. Considering the A atoms as almost neutral in the clathrates would thus correspond to a model where the charge rearrangements due to bonding in these compounds is ignored and net charges are assigned only on the basis of the changes due to the superposition of frozen atomic clouds. A multiwavelength diffraction experiment, also reported in Ref. [11], supports the QTAIM view of ionized guests in clathrates. It finds similar oxidation states for the Sr atoms in the different cages and an adsorption edge close to that found in the Sr K-edge XANES

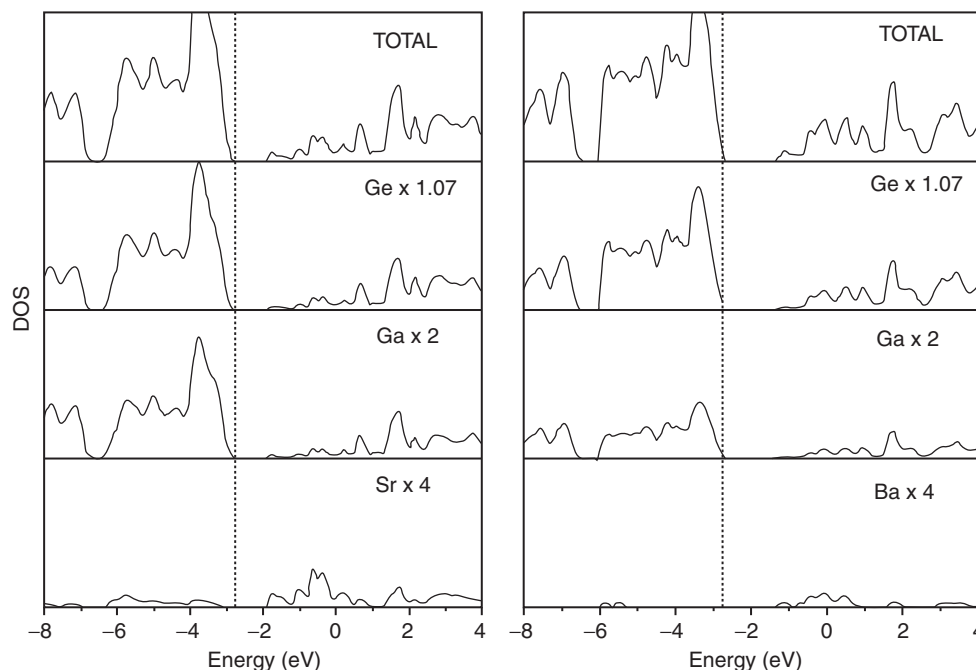


**FIGURE 7.2** Total density of states (DOS) and their atomic projections on the different sets of contributing atoms (Ge, Ga, A) for  $A_8Ga_{16}Ge_{30}$  (left: A = Sr; right: A = Ba), at minimum energy geometries and near the Fermi level.<sup>6</sup> The scale factor for each projection is designed to compare on the same scale the average single-atom contribution to the DOS from each set. The Fermi level is indicated as a vertical dashed line.

spectra of  $\text{Sr}(\text{OH})_2 \cdot 8\text{H}_2\text{O}$ . Density of states (DOS) and their atomic projections on the different sets of contributing atoms (Ge, Ga, A) for Ba and Sr clathrate, are portrayed in Figure 7.2. Sr and Ba both provide negligible contributions to valence states close to the Fermi level, but dominate the conduction states close to this level. This confirms that the guest atoms act as *charge donors*. Electrons are transferred from the highest valence bands of  $\text{A}_8$  sublattice and placed into empty orbitals of the  $\text{Ga}_{16}\text{Ge}_{30}$  sublattice. The authors' approach thus reconciles theory with the Zintl phase view of the clathrates by describing the guest atoms as highly ionized charge donors.<sup>11</sup>

QTAIM was also used to discuss<sup>11</sup> changes in bonding when the idealized, fully symmetric  $Pm\text{-}3n$  structure, having all Ga atoms in 16i positions, is relaxed to the most and the second most stable P1 structures detailed above. Geometry relaxation yields to a significant displacement of Sr and Ba atoms from the center of the 20-atom cages and to a greater extent from the center of the 24-atom cages (0.81 and 0.42 Å for Sr and Ba, respectively).<sup>8</sup>

Interestingly, the physical origin for this guest atom disorder is due to energy gain obtained when many weak guest–host bonds in the fully symmetrical clathrate cage are replaced by fewer much stronger and shorter chemical bonds in the asymmetrical case (Figure 7.3).<sup>11</sup> This is detailed in Table 7.2, which illustrates that a larger density value at the bond critical point (bcp),<sup>4</sup> results in a stronger guest–host interaction. In the large cages, only 2.8(8) and 4.0(11) guest–frame bonding interactions are found on average for the Sr and Ba clathrates, respectively, compared to the eight equal bonds present in the  $Pm\text{-}3n$  structure. The few remaining interactions are however notably stronger as suggested by the 50% (Sr) and 16% (Ba) average increases in the electron density at the bcp,  $\rho_b$ , with respect to the  $\rho_b$  values in the fully symmetrical clathrate.

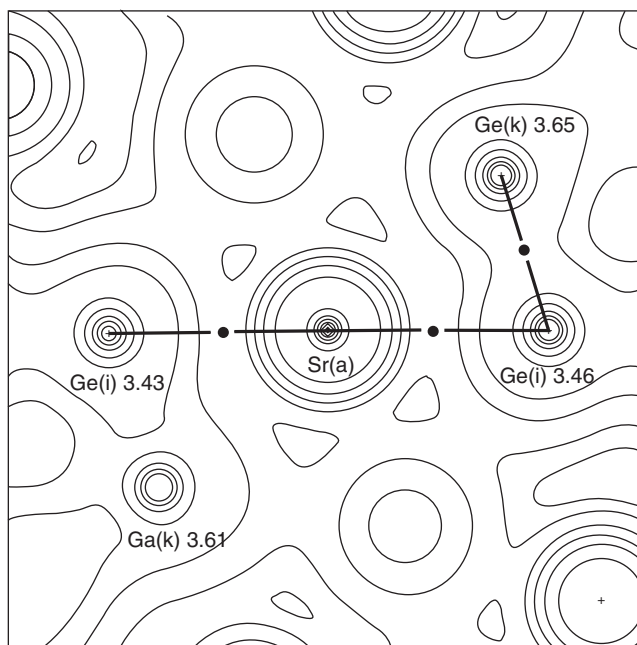


**FIGURE 7.3**  $\text{Sr}_8\text{Ga}_{16}\text{Ge}_{30}$  clathrate at minimum P1 geometry: contour map of the *ab initio* pseudo-potential electron density in a plane containing an Sr atom at a position a (20-atom cage) and two Ge atoms at positions i and k at distances of 3.46 and 3.65 Å from the Sr atom. Positions are labeled according to  $Pm\text{-}3n$  space group. The nuclei of the Ge and Ga atoms at the left of the central Sr atom are less than 0.1 Å from the plotted plane. The overlaid bond paths denote the Ge atom bonded to the Sr atom, with black dots marking the positions of bond critical points. According to QTAIM, the Ge and Ga atoms at k positions and with distances from Sr greater than 3.6 Å, are not bonded to the central Sr atom.

**TABLE 7.2** Guest–Frame-Bonding Interactions in the Idealized, Fully Symmetric  $Pm\text{-}3n$  Space Group and in the Minimum Energy Geometry  $P1$  Space Group  $A_8Ga_{16}Ge_{30}$  ( $A = \text{Sr}, \text{Ba}$ ) Clathrates

Space Group/Cage	Bond, A–B	$N^a$	$R_{A-B}$ (Å)	$(\rho_b \times 10^2)^b$
$Pm\text{-}3n/20$	Sr(2a)-Ga(i)	8	3.48	0.99
$Pm\text{-}3n/20$	Sr(2a)-Ge(k)	12	3.61	0.95
$Pm\text{-}3n/24$	Sr(6d)-Ge(k)	8	3.66	0.82
$P1/20$	Sr-Ge,Ga	8 (0)	3.46 (2)	1.03 (5)
$P1/24$	Sr-Ge,Ga	2.8 (8)	3.38 (7)	1.24 (13)
$Pm\text{-}3n/20$	Ba(2a)-Ga(i)	8	3.51	1.12
$Pm\text{-}3n/20$	Ba(2a)-Ge(k)	12	3.63	1.08
$Pm\text{-}3n/24$	Ba(6d)-Ge(k)	8	3.69	0.93
$P1/20$	Ba-Ge,Ga	13 (0)	3.54 (6)	1.15 (8)
$P1/24$	Ba-Ge,Ga	4.0 (11)	3.59 (13)	1.08 (16)

For the  $P1$  symmetry clathrate, bond properties are averaged over cages of a given type. Standard deviations are reported in parentheses. Data from Ref. [11], all quantities in atomic units, if not otherwise stated.

<sup>a</sup>  $N$  is the (average) multiplicity of each interaction.

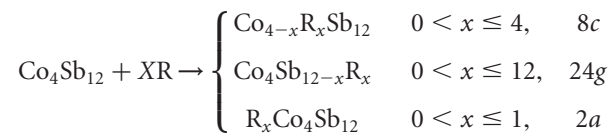
<sup>b</sup> Electron density at the bond critical point.

The strength of bonding interactions have been recently related to, and correspond to the higher rattling frequencies<sup>12</sup> in  $\text{Sr}_8\text{Ga}_{16}\text{Ge}_{30}$  (compared to  $\text{Ba}_8\text{Ga}_{16}\text{Ge}_{30}$ ). The same relationship is observed in the large rather than in the small cages of Sr clathrate (the opposite being true for Ba).<sup>10</sup> Vibrational frequencies were derived from a local Einstein model which describes the temperature dependence of the atomic displacement factors obtained in recent high resolution synchrotron powder diffraction and in single crystal neutron diffraction experiments.<sup>10</sup>

### 7.3 Theoretical Modeling for Optimal Doping Elements and Doping Level in $\text{Co}_4\text{Sb}_{12}$

The narrow bandgap semiconductors like  $\text{Co}_4\text{Sb}_{12}$  are a natural starting point in the search of good TE materials due to their favorable electronic transport properties (high  $\alpha$  and  $\sigma$ ). However, the thermal conductivity in  $\text{Co}_4\text{Sb}_{12}$  is very high and nanostructuring or doping induced structural/electronic modifications are required for competitive applications. The binary skutterudite  $\text{Co}_4\text{Sb}_{12}$  belongs to the cubic space group  $\text{Im-}3$ . Cobalt atoms occupy the 8c positions, and form a cubic lattice whose voids are partially filled by  $\text{Sb}_4$  rings and where antimony occupies the 24g positions. The 2a positions, at the center of the remaining cubic voids, can be partially filled by loosely bound “rattling” atoms<sup>\*12</sup> which raise the local anharmonic phonon modes and consequently lower  $\lambda_L$ .

In  $\text{Co}_4\text{Sb}_{12}$  the doping element R can occupy three different crystallographic sites:



If an electron donor element R occupies the interstitial position 2a, the material becomes an  $n$ -doped semiconductor with negative  $\alpha$  values, whose magnitudes depend on the chemical nature and concentration of the defective atom. By contrast, when R occupies a frame position (8c or 24g), the resulting material is either  $n$ - or  $p$ -doped according to the number of valence electrons provided by R as compared to the substituted atom.

<sup>\*</sup>A rattler atom is one which is bound in an oversized atomic cage of a given material. Its presence can cause a lowering of the lattice thermal conductivity with little or no effect on the electronic transport properties.

A detailed knowledge of the structure is a fundamental prerequisite for understanding the bulk properties of a material, and a concise example is represented by the Te-doped  $\text{Co}_4\text{Sb}_{12}$  system.<sup>13</sup> Te atoms should substitute Sb atoms yielding  $\text{Co}_4\text{Sb}_{11-x}\text{Te}_x$ , but they might also occupy the 2a position, providing the filled system  $\text{Te}_x\text{Co}_4\text{Sb}_{12}$ . Te substitution for Sb is hardly detectable by conventional XRD techniques, because the two elements have very similar scattering factors. Therefore, in order to accurately determine where the Te atoms preferentially sit in the material, the electronic structure of  $\text{Co}_4\text{Sb}_{11}\text{Te}$  and  $\text{TeCo}_4\text{Sb}_{12}$  is evaluated. In the former system, the computed Seebeck coefficient is negative and increases in magnitude almost linearly with  $T$  (see Figure 7.4), in agreement with the available experimental findings.<sup>14</sup> By contrast, the Seebeck coefficient is much lower in magnitude in  $\text{TeCo}_4\text{Sb}_{12}$ , and it becomes even positive below 400 K in this system. The computed trends of  $\alpha$  may thus be used as a tool for selecting a structure after doping.<sup>15</sup> The above-cited case illustrates this where one may safely conclude that Te atoms should sit mainly on the Sb sites and also illustrates the impact of actual structure on bulk properties such as the Seebeck coefficient.

In addition, the relationship of location, atomic nature and concentration of the dopant atom to the resulting electronic transport properties in a series of doped cobalt antimonides was investigated. It is well known from the literature that  $n$ -doping has a positive effect on the TE properties of  $\text{Co}_4\text{Sb}_{12}$ , and therefore we considered Ni,<sup>16,17</sup> Te,<sup>14</sup> Ba,<sup>18</sup> and La<sup>19</sup> as electron donors. Ba and La are filler atoms and occupy 2a positions, while Te and Ni<sup>20</sup> substitute Sb and Co, respectively.

The authors determined the electronic band structure of  $\text{Co}_3\text{NiSb}_{12}$ ,  $\text{Co}_4\text{Sb}_{11}\text{Te}$ ,  $\text{BaCo}_4\text{Sb}_{12}$ , and  $\text{LaCo}_4\text{Sb}_{12}$ , and thereby included expressly the perturbation of the band structure of  $\text{Co}_4\text{Sb}_{12}$  due to the inserted atom, although retaining the Im-3 space group symmetry constraint. Analysis of the DOS and of their atomic projections on the different sets of contributing atoms (Figure 7.5) reveals the changes induced on the electronic structure by the different dopant atoms and sites considered. Substitution of Sb with Te leaves the DOS shape substantially unchanged as the electronic states of Te nearly replace those of the removed Sb. This same behavior is observed when Ni is substituted for Co (not shown in Figure 7.5). Contributions of Ba filler to the total DOS around the Fermi level are scarce and Ba acts essentially as an electron supplier. Instead, the La filler contributes significantly to the states close to the Fermi level through a greater mixing of its  $d$  states with both the valence and conduction states of  $\text{Co}_4\text{Sb}_{12}$ . Therefore, it is not acting as a simple electron donor.

These different DOS portraits, along with changes in the Fermi level position and dispersion and velocity of bands around the Fermi level, have important consequences on the electronic transport properties of these doped systems. The Seebeck coefficient and electrical conductivity trends at 300 K (as a function of the dopant atom content and within the frozen band model) starting from the band structures of the fully doped systems are displayed in Figure 7.6. The frozen band approach was also applied to the band structure of  $\text{Co}_4\text{Sb}_{12}$ . This corresponds to disregarding any band perturbation induced by doping and distinguishing doping elements solely on the basis of their formal capability to

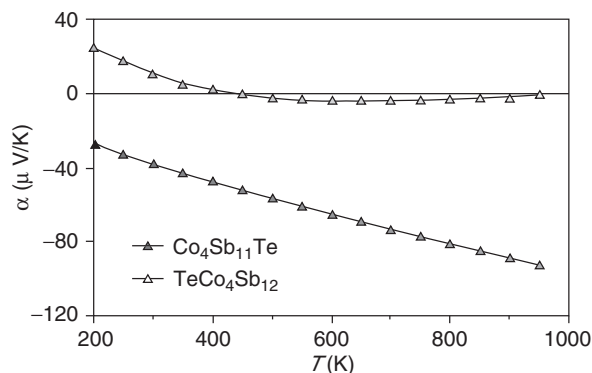
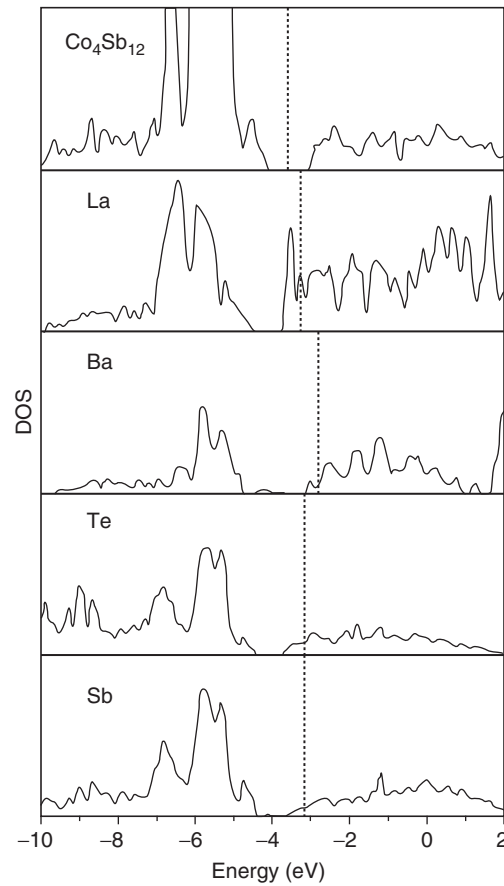
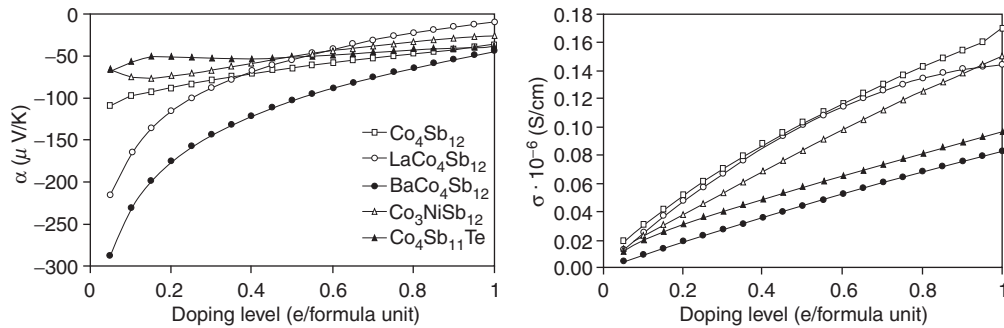


FIGURE 7.4 Seebeck coefficient  $\alpha$  for  $\text{TeCo}_4\text{Sb}_{12}$  and  $\text{Co}_4\text{Sb}_{11}\text{Te}$  as a function of the absolute temperature  $T$ .





**FIGURE 7.5** Atom projected density of the states (DOS) for Ba and La in the fully filled Co<sub>4</sub>Sb<sub>12</sub> systems, and for Te and Sb in Co<sub>4</sub>Sb<sub>11</sub>Te. The Co<sub>4</sub>Sb<sub>12</sub> total DOS, scaled by a factor 1/12, is reported for the sake of comparison. The Fermi level is indicated as a vertical dashed line.



**FIGURE 7.6** Seebeck coefficient  $\alpha$ , left panel, and electrical conductivity  $\sigma$ , right panel, at 300 K, as a function of the  $n$ -doping level respect to undoped Co<sub>4</sub>Sb<sub>12</sub>. The frozen band approach and the band structure of the fully doped ( $x = 1$ ) systems were used.



**TABLE 7.3** Best Doping Levels for  $R_x\text{Co}_4\text{Sb}_{12}$  ( $R = \text{Ba}, \text{La}$ ),  $\text{Co}_{4-x}\text{Ni}_x\text{Sb}_{12}$  and  $\text{Co}_4\text{Sb}_{12-x}\text{Te}_x$  at 300 K According to the Maximal Power Factor ( $\alpha^2\sigma$  in  $\mu\text{W/K}^2\text{cm}$ ) Criterion and Using Various Band Structures in the Frozen Band Approach (Constant Relaxation Time  $\tau = 10^{-14}$  sec)

Band Structure	$n$	$x$	$\alpha$	$\alpha^2\sigma$	$Z_e T$	$x_{\text{Exp}}$	$ZT_{\text{Exp}}$
$\text{Co}_4\text{Sb}_{12}$	0.35		-73.7	330	1.4		
$\text{BaCo}_4\text{Sb}_{12}$	-0.22	0.11	-166.9	570	4.0	0.16 <sup>a</sup>	0.24
$\text{LaCo}_4\text{Sb}_{12}$	-0.15	0.05	-134.9	680	3.5	0.05 <sup>b</sup>	0.13
$\text{Co}_3\text{NiSb}_{12}$	-0.32	0.32	-64.4	230	1.2		
$\text{Co}_4\text{Sb}_{11}\text{Te}$	-0.58	0.58	-49.1	160	0.9	0.24 <sup>c</sup>	0.11

The doping level  $n$  is reported as negative for  $p$ -doped and as positive for  $n$ -doped systems with respect to the reference system (column 1).  $Z_e T$  is the adimensional electronic figure of merit.  $x_{\text{Exp}}$  and  $ZT_{\text{Exp}}$  are the experimental best doping level according to measured  $\alpha^2\sigma$  and the corresponding figure-of-merit at 300 K.

<sup>a</sup> Ref. [18].

<sup>b</sup> Ref. [19].

<sup>c</sup> Ref. [14].

supply electrons to the system, with respect to  $\text{Co}_4\text{Sb}_{12}$ . At low dopant content, the two structures with atoms at 2a position show much higher  $\alpha$  magnitudes than the frame substituted structures, which display similar trends to “physically” doped  $\text{Co}_4\text{Sb}_{12}$ . The Ba filler is definitely more effective than La filler in enhancing thermopower. The electrical conductivity, using a constant relaxation time  $\tau$  of  $10^{-14}$  sec for all systems, increases almost linearly with the doping level (except  $\text{LaCo}_4\text{Sb}_{12}$ ). Ba-filled system exhibited the lowest conductivity values.

As expected,  $\alpha$  changes do not parallel  $\sigma$  changes. We evaluated the optimal doping level for each dopant in order to determine which dopant yielded the maximum value of the power factor  $\alpha^2\sigma$  against the charge carrier concentration, at a fixed temperature, and using the frozen band approach. Results are displayed in Table 7.3, along with the corresponding transport properties, while the dependence of the power factor on the doping level is shown in Figure 7.7. The optimal levels are distributed in the wide range of 0.15 to 0.58 e/formula unit and differ significantly from those obtained by doping  $\text{Co}_4\text{Sb}_{12}$ . This further reveals that the dopant atoms do not act as simple electron suppliers, but they rather play an important role in defining the electronic band structure.

As a final step in our analysis, we introduced the *electronic* figure-of-merit,  $Z_e T = (\alpha^2\sigma/\lambda_e)T$ , which is an upper bound ( $\lambda_L = 0$ ) to the total figure-of-merit.  $Z_e T$  has the advantage of being independent on the relaxation time (while  $\alpha^2\sigma$  is not) when the electric current and the thermal current relaxation times are assumed to be equal. Because of this,  $Z_e T$  is conveniently used to estimate trends in total  $ZT$ , once the optimal doping level has been obtained from  $\alpha^2\sigma$  for a series of related systems. Our results are qualitatively consistent with the experimental findings.<sup>14,16–19</sup> The dopant atoms in the frame (Ni, Te)

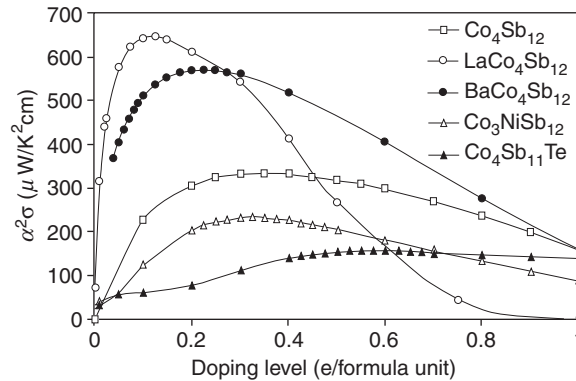


**FIGURE 7.7** Power factor  $\alpha^2\sigma$  at 300 K as a function of the  $n$ -doping level with respect to undoped  $\text{Co}_4\text{Sb}_{12}$ .

were found less effective than the filler atoms in improving the total figure-of-merit, and, between fillers, Ba was a more effective filler than La.

This study sheds some light on how the electronic transport properties of doped  $\text{Co}_4\text{Sb}_{12}$  heavily depend on the band structure perturbations induced by the nature and location of the dopants, despite several crude assumptions we made in the modeling: Im-3 structure, single-cell calculations, semi-classical treatment of transport within frozen band approach, constant and equal relaxation time for all systems and doping levels. Further insight into the TE properties of these doped compounds awaits an evaluation of those phonon features which affect their thermal transport.

## 7.4 A Combined Theoretical and Experimental Structural Study of $\beta$ Zn–Sb

The thermoelectric properties of Zn–Sb alloys are very promising and strongly depend on their specific phases and exact composition.<sup>21,22</sup> Caillat et al.<sup>23</sup> measured a  $ZT$  of 1.3 at 670 K for a  $p$ -doped sample of the  $\beta$  phase (formal stoichiometry  $\text{Zn}_4\text{Sb}_3$ ), which is a promising substitute for Pb–Te alloys because it has a higher  $ZT$ , and it is lead-free. The Seebeck coefficient and the electrical conductivity in  $\text{Zn}_4\text{Sb}_3$  are not exceptionally high, and the very high  $ZT$  is due to the unusually low lattice part of the thermal conductivity. A recent XRD study<sup>24</sup> suggests that the very low  $\lambda_L$  is due to interstitial zinc atoms inside the crystalline lattice. The discovery of Zn interstitials provides for the first time a crystalline structure model which is consistent with the measured mass density and provides a novel scattering mechanism for the phonons. A previous experimental<sup>25</sup> study proposed a site with mixed Zn/Sb occupancy to conform with the experimental composition, and did not recover any Zn interstitials. The only theoretical investigation<sup>26</sup> on  $\text{Zn}_4\text{Sb}_3$  proposed an even simpler model structure which contained neither mixed occupation sites nor Zn interstitials. In this earlier study, a proper doping using the frozen band approach was used to reproduce the experimental transport properties.

We summarize here our *ab initio* investigation<sup>27</sup> aimed at deconvolving the structural information from the space–time averaged electron density of a  $\text{Zn}_4\text{Sb}_3$  sample, which was obtained from a Rietveld/MEM analysis of powder diffraction (PD) data. These data confirm and quantitatively improve the structural description given by the recent XRD study.<sup>24</sup> The crystal space group is R-3c (trigonal setting) and the antimony sits in 6e and 4c positions with unit occupancy. Therefore, every cell contains ten Sb atoms in well-defined sites. In contrast, the zinc atoms are distributed over four 12f positions indicated with the capital letters A to D, and having the following fractional occupancy: 0.899 (A), 0.068 (B and C), and 0.033 (D). The resulting stoichiometry is  $\text{Zn}_{12.816}\text{Sb}_{10}$ .

The discovery of several Zn sites with fractional occupancy indicates the presence of disorder, point or extended defects within the sample. Therefore, the instantaneous location and number of zinc atoms in the cells remain unknown. The target of our study is to determine the most stable structures composing the system, to account for the experimental stoichiometry, and to establish whether interstitial Zn atoms affect the TE properties of this material.

Among the large number of possible structures given by combination of the 48 experimental zinc positions, we selected a limited number of candidate structures using simple physical criteria which included geometrical constraints on Zn–Zn distances and relative energies of the structures, obtained from total energy computations. Surprisingly we found that the overall structure is very simple, and presents just three different cell arrangements. The sample consists of the highly symmetrical framework  $\text{A}_{12}\text{Sb}_{10}$  and defective modifications obtained from it (see Figure 7.8), which conforms to the experimental dominant occupation of the A site. As the  $\text{A}_{12}\text{Sb}_{10}$  cells cannot host interstitial zinc atoms, the most favored defect is obtained by creating a zinc vacancy and placing one B and one C atoms in its cavity, generating  $\text{A}_{11}\text{BCSb}_{10}$ . The inserted atoms form a dimer with internuclear distance 2.23 Å, and the stability of the dimers validates that the occupancies of the B and C sites were constrained to be equal after a refined examination of the PD data. The clustering among dimers is largely unfavorable, and thus they represent point defects and do not form extended domains. Furthermore, the crystal cells containing

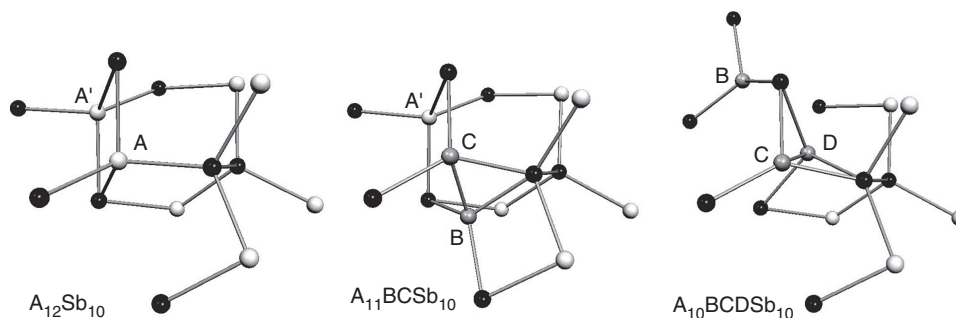


**FIGURE 7.8** Stick-and-ball representation of the structures composing the  $\text{Zn}_4\text{Sb}_3$  crystal. Antimony atoms are painted in black; zinc atoms in A positions in light gray; defective zinc atoms (B, C and D positions) in dark gray. Left panel: the nondefective framework. Middle panel: a zinc vacancy is created in the A position, and a BC zinc dimer is inserted. Right panel: the rearrangement of the zinc framework involving the dimer and the zinc atom in A.

dimers may rearrange, displacing one zinc atom from the A to the D position to generate  $\text{A}_{10}\text{BCDSb}_{10}$ . The most stable among the possible arrangements of these cells, plotted in Figure 7.8, is just 7 kcal/mol more unstable compared to  $\text{A}_{11}\text{BCSb}_{10}$ . This quasi degeneracy is consistent with the experimental outcome that there is about one D atom on every two dimers. Finally, the experimental stoichiometry is exactly reproduced as a 0.184:0.420:0.396 mixture of  $\text{A}_{12}\text{Sb}_{10}$ ,  $\text{A}_{11}\text{BCSb}_{10}$ , and  $\text{A}_{10}\text{BCDSb}_{10}$  cells, respectively. The overall content of 12.816 Zn atoms/cell results from the mixing of cells with 12 and 13 zinc atoms, and we found no cells with different zinc content that are energy competitive, indicating that zinc is as homogeneously distributed as possible within the sample. The BC dimers are probably responsible for the very low  $\lambda_L$  observed experimentally because they introduce disorder in the symmetrical  $\text{A}_{12}\text{Sb}_{10}$  framework.

The electronic structure of  $\text{A}_{12}\text{Sb}_{10}$  is a highly *p*-doped semiconductor with a charge carriers' concentration of  $2e/\text{cell}$ , and its DOS is reported in Figure 7.9. The insertion of a zinc dimer in a crystal cell completely fills the states up to the bandgap, and the rearrangement of zinc atoms involving the D site has no relevant effects on the electronic structure (see Figure 7.9). The cells with more than 13 zinc atoms are *n*-doped semiconductors or even metals, in disagreement with the

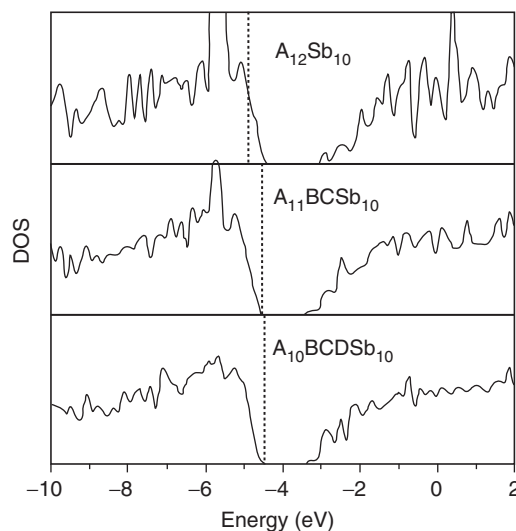


**FIGURE 7.9** Total density of states (DOS) of different zinc antimonide cells. For each system, the Fermi level is indicated by the vertical dashed line.

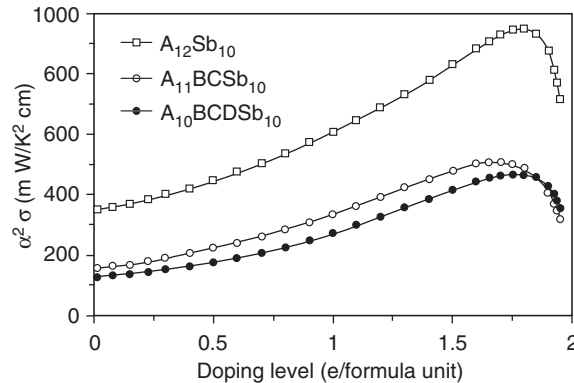


**FIGURE 7.10** Power factor  $\alpha^2\sigma$  at 700 K as a function of the doping level in the  $\beta$ -ZnSb crystal. Zero doping level corresponds to a crystal cell with stoichiometry  $\text{Zn}_{12}\text{Sb}_{10}$ ; the insertion of 2 e/cell corresponds to a 13-Zn atoms cell. The power factor is computed applying the frozen band approximation to the band structures of  $\text{A}_{12}\text{Sb}_{10}$ ,  $\text{A}_{11}\text{BCSb}_{10}$ , and  $\text{A}_{10}\text{BCDSb}_{10}$ .

experimental findings. The  $\text{A}_{12}\text{Sb}_{10}$ ,  $\text{A}_{11}\text{BCSb}_{10}$ , and  $\text{A}_{10}\text{BCDSb}_{10}$  cells have very similar DOS, and therefore zinc atoms act mainly as electron suppliers, increasing the number of available valence electrons. We modeled the real sample using the frozen band approximation, either by  $n$ -doping the 12-Zn atoms cells or by  $p$ -doping the 13-Zn ones to reproduce the experimental electron count. Placing 1.632e in  $\text{A}_{12}\text{Sb}_{10}$  or removing 0.368e in either  $\text{A}_{11}\text{BCSb}_{10}$  or  $\text{A}_{10}\text{BCDSb}_{10}$  yields similar Seebeck coefficients (+115, +123, and +110  $\mu\text{V/K}$ , respectively, at 670 K), confirming that the three band structures are actually close to each other and that the system is a  $p$ -doped semiconductor, as found experimentally. We then maximized the power factor  $\alpha^2\sigma$  at varying zinc content, and our theoretical predictions are reported in Figure 7.10. First, the insertion of zinc dimers in  $\text{A}_{12}\text{Sb}_{10}$  strongly enhances the power factor. Indeed, the insertion of four Zn dimers on every five  $\text{Zn}_{12}\text{Sb}_{10}$  cells increases  $\alpha^2\sigma$  by a factor of three. Second, the predicted optimal composition is about  $\text{Zn}_{12.85}\text{Sb}_{10}$ , which is very close to the real sample. This result is challenging since the native defects present in the sample nearly maximize the power factor, though the experimental stoichiometry does not result from any doping optimization procedure. The results obtained so far demonstrate a need for new theoretical and experimental investigations, primarily to further enhance our understanding of the role of internal (Zn) and external doping on the TE properties of this material.

## References

1. Saunders, V.R., Dovesi, R., Roetti, C., Causà, M., Harrison, N.M., Orlando, R., and Zicovich-Wilson, C.M., *CRYSTAL98 User's Manual*, University of Torino, Torino, 1998.
2. Elliott, S., *The Physics and Chemistry of Solids*, Wiley, Chichester, chap. 6, 1998.
3. Bertini, L. and Gatti, C., *ELTRAP*, CNR-ISTM, Milan, 2003.
4. Bader, R.F.W., *Atoms in Molecules: A Quantum Theory*, International Series of Monographs on Chemistry 22. Oxford University Press, Oxford, 1990.
5. Gatti, C., *TOPOND98 User's Manual*, CNR-ISTM, Milan, 1999.
6. Slack, G.A., New materials and performance limits for thermoelectric cooling. In *CRC Handbook of Thermoelectrics*, D.M. Rowe, ed. CRC Press, Boca Raton, FL, chap. 34, 1995.
7. Bryan, J.D., Blake, N.P., Metiu, H., Iversen, B.B., Poulsen, R.D., and Bontien, A., Nonstoichiometry and chemical purity effects in thermoelectric  $\text{Ba}_8\text{Ga}_{16}\text{Ge}_{30}$  clathrate, *J. Appl. Phys.*, 92, 7281, 2002.
8. Blake, N.P., Bryan, D., Lattner, S., Möllnitz, L., Stucky, G.D., and Metiu, H., Structure and stability of the clathrates  $\text{Ba}_8\text{Ga}_{16}\text{Ge}_{30}$ ,  $\text{Sr}_8\text{Ga}_{16}\text{Ge}_{30}$ ,  $\text{Ba}_8\text{Ga}_{16}\text{Si}_{30}$  and  $\text{Ba}_8\text{In}_{16}\text{Sn}_{30}$ , *J. Chem. Phys.*, 114, 10063, 2001.

9. Bentien, A., Palmqvist, A.E.C., Bryan, J.D., Latturner, S., Stucky, G.D., Furenlid, L., and Iversen, B.B., Experimental charge densities of semiconducting cage structures containing alkaline earth guest atoms, *Angew. Chem. Int. Ed.*, 39, 3613, 2000.
10. Bentien, A., Nishibori, E., Paschen, S., and Iversen, B.B., Crystal structures, atomic vibration and disorder of type I thermoelectric clathrates  $\text{Ba}_8\text{Ga}_{16}\text{Si}_{30}$ ,  $\text{Ba}_8\text{Ga}_{16}\text{Ge}_{30}$ ,  $\text{Ba}_8\text{In}_{16}\text{Ge}_{30}$ ,  $\text{Sr}_8\text{Ga}_{16}\text{Ge}_{30}$ , *Phys. Rev. B*, 71, 144107, 2005.
11. Gatti, C., Bertini, L., Blake, N.P., and Iversen, B.B., Guest-framework interaction in type I inorganic clathrates with promising thermoelectric properties: on the ionic versus neutral nature of the alkaline-earth metal guest A in  $\text{A}_8\text{Ga}_{16}\text{Ge}_{30}$  (A = Sr, Ba), *Chem. Eur. J.*, 9, 4556, 2003.
12. Sales, B.C., Mandrus, D., Chakoumakos, B.C., Keppens, V., and Thomson, J.R., Filled skutterudite antimonides: electron crystals and phonon glasses, *Phys. Rev. B*, 56, 15081, 1997.
13. Bertini, L., Billquist, K., Christensen, M., Gatti, C., Holmgren, L., Iversen, B.B., Mueller, E., Muhammed, M., Noriega, G., Palmqvist, A., Platzek, D., Rowe, D.M., Saramat, A., Stiewe, C., Toprak, M., Williams, S.G., and Zhang, Y., Theoretical modeling of Te doped  $\text{CoSb}_3$ , *Proceedings of the 22nd International Conferences of Thermoelectric*, 23, 85, 2004.
14. Wojciechowski, K., Toboła, J., and Leszczyński, J., Thermoelectric properties and electronic structure of  $\text{CoSb}_3$  doped with Se and Te, *J. Alloy Compd.*, 361, 19, 2003.
15. Bertini, L. and Gatti, C., The impact of the actual geometrical structure of a thermoelectric material on its electronic transport properties. The case of doped skutterudite systems, *J. Chem. Phys.*, 121, 8983, 2004.
16. Dyck, J.S., Chen, W., Yang, J.H., Meisner, G.P., and Uhrer, C., Effect of Ni on the transport and magnetic properties of  $\text{Co}_{1-x}\text{Ni}_x\text{Sb}_3$ , *Phys. Rev. B*, 65, 115204, 2002.
17. Bertini, L., Stiewe, C., Toprak, M., Williams, S., Platzek, D., Mroczek, A., Zhang, Y., Gatti, C., Mueller, E., Muhammed, M., and Rowe, D.M., Nanostructured  $\text{Co}_{1-x}\text{Ni}_x\text{Sb}_3$  skutterudites: synthesis, thermoelectric properties, and theoretical modeling, *J. Appl. Phys.*, 93, 438, 2003.
18. Chen, L.D., Kawahara, T., Tang, X.F., Goto, T., Hirai, T., Dyck, J.S., Chen, W., and Uhrer, C., Anomalous barium filling fraction and *n*-type thermoelectric performance of  $\text{Ba}_y\text{Co}_4\text{Sb}_{12}$ , *J. Appl. Phys.*, 90, 1864, 2001.
19. Nolas, G.S., Cohn, J.L., and Slack, G.A., Effect of partial void filling on the lattice thermal conductivity of skutterudites, *Phys. Rev. B*, 58, 164, 1998.
20. Christensen, M., Iversen, B.B., Bertini, L., Gatti, C., Toprak, M., Muhammed, M., and Nishibori, E., Structural study of Fe doped and Ni substituted thermoelectric skutterudites by combined synchrotron and neutron powder diffraction and *ab initio* theory, *J. Appl. Phys.*, 96, 3148, 2004.
21. Izard, V., Record, M.C., Tedenac, J.C., and Fries, S.G., Discussion of the stability of the antimony–zinc binary phases, *Calphad Comput. Coupling Phase Diagrams Thermochem*, 25, 567, 2001.
22. Zhang, L.T., Tsutsui, M., Ito, K., and Yamaguchi, M., Effects of  $\text{ZnSb}$  and  $\text{Zn}$  inclusions on the thermoelectric properties of  $\beta\text{-Zn}_4\text{Sb}_3$ , *J. Alloy. Compd.*, 358, 252, 2003.
23. Caillat, T., Fleurial, J.-P., and Borshchevsky, A., Preparation and thermoelectric properties of semiconducting  $\text{Zn}_4\text{Sb}_3$ , *J. Phys. Chem. Solids*, 58, 1119, 1997.
24. Snyder, G.J., Christensen, M., Nishibori, E., Caillat, T., and Iversen, B.B., Disordered zinc in  $\text{Zn}_4\text{Sb}_3$  with phonon-glass and electron-crystal thermoelectric properties, *Nat. Mater.*, 3, 458, 2004.
25. Mayer, H.W., Mikhail, I., and Schubert, K., Über einige phasen der mischungen  $\text{ZnSb}_N$  und  $\text{CdSb}_N$ , *J. Less-Common Metals*, 59, 43, 1978.
26. Kim, S.-G., Mazin, I.I., and Singh, D.J., First-principles study of Zn–Sb thermoelectrics, *Phys. Rev. B*, 57, 6199, 1998.
27. Cargnoni, F., Nishibori, E., Rabiller, P., Bertini, L., Snyder, G.J., Christensen, M., Gatti, C., and Iversen, B.B., Interstitial Zn atoms do the trick in thermoelectric zinc antimonide,  $\text{Zn}_4\text{Sb}_3$ : a combined maximum entropy method X-ray electron density and *ab initio* electronic structure study, *Chem. Eur. J.*, 10, 3862, 2004.